Journal of Alloys and Compounds 944 (2023) 169206

Contents lists available at ScienceDirect

Journal of Alloys and Compounds

journal homepage: www.elsevier.com/locate/jalcom

A multifunctional nanoplatform based on Fe_3O_4@Au NCs with magnetic targeting ability for single NIR light-triggered PTT/PDT synergistic therapy of cancer

Tianxiang Zhou [a], Jie Huang [a], Wenshi Zhao [a,b,c], Rui Guo [a], Sicheng Cui [a], Yuqing Li [a], Naveen Reddy Kadasala [d], Yuhong Jiang [a], Yang Liu [a,*], Qi Zhang [a,*]

[a] Key Laboratory of Functional Materials Physics and Chemistry of the Ministry of Education, Jilin Normal University, Changchun 130103, PR China
[b] Changchun Institute of Optics, Fine Mechanics and Physics, Chinese Academy of Sciences, Changchun 130033, PR China
[c] University of Chinese Academy of Sciences, Beijing 100049, PR China
[d] Department of Chemistry, Towson University, Towson, MD 21252, United States

ARTICLE INFO

Article history:
Received 26 July 2022
Received in revised form 31 January 2023
Accepted 6 February 2023
Available online 7 February 2023

Keywords:
Photothermal therapy
Photodynamic therapy
Fe_3O_4 @Au nanocomposites
Synergistic effect
Magnetic targeting

ABSTRACT

Although simultaneous photothermal therapy (PTT) and photodynamic therapy (PDT) have been proven to be beneficial for cancer treatment, high-power laser light sources, shallow penetration depth of light and especially activation by two different light sources make it difficult to be popularized in clinical cancer therapy. Herein, the novel multifunctional Fe_3O_4 @Au nanocomposites (NCs) have been designed and synthesized, which simultaneously act as photothermal conversion agents (PCAs) and photosensitizers (PSs) for PTT/PDT synergistic therapy of human cervical cancer (HeLa) cells using a single excitation light source. Under low-power 808 nm laser irradiation, photothermal conversion efficiency (PCE) of Fe_3O_4 @Au NCs was as high as 39.22% and the cytotoxic singlet oxygen ($^1O_2$) could be simultaneously generated. In addition, Fe_3O_4 @Au NCs showed relatively good biocompatibility and low cytotoxicity, which were ideal alternatives for nanotherapeutic agents for treatment of HeLa cells. Meanwhile, PTT only and PTT/PDT dual-modal therapeutic effects of Fe_3O_4 @Au NCs on HeLa cells were compared. The experimental results confirmed that the near-infrared (NIR)-triggered PDT/PTT synergistic therapy of HeLa cells was more efficient due to the synergistic effect. Interestingly, Fe_3O_4 @Au NCs with saturation magnetization (Ms) value of 66.5 emu/g possessed good magnetic responsivity, which could be collected easily with a magnet. The magnetic targeting of Fe_3O_4 @Au NCs could effectively promote their accumulation at tumor sites, thus further enhancing the efficacy of PTT/PDT synergistic therapy of HeLa cells. This study provides a feasible paradigm for magnetic targeting-assisted PTT/PDT synergistic therapy of cancer cells under a single-wavelength excitation and opens up a novel direction for clinical cancer therapy.

1. Introduction

Cancer is one of the malignant neoplasms manifested as the unbounded division and development of aberrant cells [1]. And cancer with risk of high incidence and mortality rates has become a widespread and ever-growing public health issue in developed and developing countries [2]. According to GLOBOCAN 2020 database released via International Agency for Research on Cancer (IARC), the number of new cancer patients was 19.3 million and the number of cancer deaths was nearly 10 million in 2020 [3]. Up to now, with deepening understanding of cancer and update of treatment concepts, multifarious cancer treatment techniques have been explored, including surgery, chemotherapy, radiotherapy, etc [4]. Although these traditional methods have certain positive significance for cancer treatment, they also have their inherent shortcomings. For example, surgery is the preferred local treatment option only for patients with early-stage cancer, and the postoperative recurrence and the metastasis of cancer cells are unpredictable or even inevitable in the vast majority of patients [5]. Chemotherapy is another common way to treat cancer, but chemotherapeutic drugs can harm healthy tissue cells while inactivating cancer cells owing to the non-selective recognition ability of chemotherapeutic drugs [6]. In addition, radiotherapy is also accompanied by a series of complications and certain side effects [7]. Consequently, there is an urgent need

* Corresponding authors.
E-mail addresses: liuyang@jlnu.edu.cn (Y. Liu), qzh7512@126.com (Q. Zhang).

https://doi.org/10.1016/j.jallcom.2023.169206
0925-8388/

but it remains a significant challenge to explore novel, effective and low side-effect therapy for cancer treatment.

Near-infrared (NIR) light induced phototherapy, primarily consisting of photothermal therapy (PTT) and photodynamic therapy (PDT), is universally recognized as the most hopeful minimally invasive treatment means for cancer at present [8–12]. Given that the heat resistance of healthy cells is higher than that of tumor cells, PTT can cause relatively little damage to normal cells and achieve the local treatment of advanced tumors [13–16]. From the theoretical point of view, PTT enables the photothermal conversion agents (PCAs) to produce local hyperthermy at tumor sites under NIR light irradiation so as to realize the purpose of photothermal ablation of tumor cells [17–23]. By contrast, PDT utilizes a laser source of a particular wavelength to trigger the photosensitizers (PSs) to produce cytotoxic reactive oxygen species (ROS), mainly involving singlet oxygen ($^1O_2$), hydroxyl radicals (•OH) and superoxide (O_2^-) ions, which can undergo oxidative reactions with adjacent cellular components, produce the cytotoxic effects and thereby induce apoptosis and necrosis of cancerous cells [24–29]. It must be mentioned that PTT and PDT have their own disadvantages. PTT may not completely eliminate tumor cells, especially marginal tumor cells, owing to the inadequate heat and uneven heat distribution [30–33]. The high laser powers are required for PTT, but hyperthermia is likely to lead to heat shock [34,35]. In addition, the shallow tissue penetration of NIR light restricts practical clinical utilization of PTT [36]. Although PDT can overcome the problem of poor light penetration into tumor tissues excited by X-rays, the hypoxia microenvironment in solid tumors still significantly influences the therapeutic efficacy of PDT [37,38].

More recently, many researchers have found that the synergistic PTT/PDT treatment for cancer therapy by combining PTT and PDT is more effective than single PTT or PDT, which should be the development trend for cancer treatment [39]. On one hand, the photothermal effect of PTT can boost the transport of PTT/PDT agents, accelerate blood circulation, and thus enhance the oxygen supplement in the tumor tissues, thereby facilitating the therapeutic effect of PDT [40]. On the other hand, produced ROS during the PDT process can inhibit the induction of heat-shock proteins, which will minimize their protective effects in tumor tissues during the PTT treatment [41]. Therefore, the synergistic PTT/PDT therapy can realize the goal that the whole is greater than the sum of its parts. Unfortunately, since the spectra of photothermal agents and PSs are mismatched, the two different light sources are usually required to activate the dual-modal phototherapeutic system, which results in a tedious treatment process and longer treatment time [42]. Therefore, it remains challenging to develop a PTT/PDT dual-modal therapeutic agent which can induce local hyperthermia and ROS simultaneously under single laser irradiation.

In the nanomedical field, noble metal nanoparticles (NPs) have particular advantages in preparation and innovation of multifunctional and multimodal nanotherapeutic agents because of their adjustable surface properties, easy functionalization and modification, excellent localized surface plasmon resonance (LSPR) effect and high electron density, which have been widely used in miscellaneous therapeutic platforms [43–46]. Among all the noble metal NPs, Au NPs have always been the preferred materials at the cutting edge of nanobiotechnology and nanomedicine because of their inherent biocompatibility, non-toxic property, non-immunogenicity, good chemical stability and strong capacity of light absorption in the NIR region [47–50]. Notably, the LSPR induced by the collective oscillation of surface electrons enables Au NPs to act simultaneously as effective PCAs and PSs, which makes it possible to achieve synergistic PTT/PDT therapy under short-term irradiation of single-wavelength NIR laser [42,51]. Furthermore, it is also indispensable to achieve precise and selective localization of nanotherapeutic agents in the synergistic therapeutic of cancer. In addition to the passive targeting of some nanotherapeutic agents achieved through enhanced permeability and retention (EPR) effect, researchers have committed to developing more valid methods to achieve efficient active targeted therapy [52,53]. At present, magnetic targeting has been widely recognized as an ideal targeting technology [54]. Firstly, the magnetic targeting exhibits good controllability and predictability under the stimulation of external magnetic field, which can achieve specific delivery without changing the nature of the internal environment. Secondly, the magnetic targeting can induce effective rapid accumulation of magnetic materials at tumor sites and thus reduce damage to normal tissues [52–54]. It is worthwhile mentioning that the combination of magnetic NPs, especially superparamagnetic magnetite Fe_3O_4, and Au NPs can not only overcome disadvantages of less accumulation of PSs in tumor tissues, but also avoid using excessive laser power and thereby widen the range of the clinical application of phototherapy [55–57].

In order to realize efficient PTT/PDT synergistic treatment of tumors with few side effects under low-power 808 nm laser irradiation, herein, the novel multifunctional Fe_3O_4 @Au nanocomposites (NCs) were designed and synthesized by a modified seed-mediated growth method (Scheme 1). Specifically, due to the superparamagnetic nature of Fe_3O_4 cores and the presence of Au shells, the well-designed Fe_3O_4 @Au NCs could be employed as ideal nanotherapeutic agents and they could permeate into and accumulate in tumor regions via EPR effect. Furthermore, Fe_3O_4 NPs endowed Fe_3O_4 @Au NCs with targeting ability, which would further promote distribution of nanotherapeutic agents in cancer cells with an external magnetic field and thus reduce damage of PTT/PDT to healthy cells. After irradiating low-dose Fe_3O_4 @Au NCs with 808 nm laser, both NIR light-triggered local hyperthermia and the generated $^1O_2$ could inhibit tumor growth and even lead to tumor ablation at mild temperatures, which realized PTT/PDT dual-modal therapy of tumors. Furthermore, the influence of magnetic targeting on PTT/PDT synergistic therapy was systematically assessed via monitoring cell viability of human cervical cancer (HeLa) cells in the presence of an external magnetic field. Therefore, our study clearly demonstrates that Fe_3O_4 @Au NCs, as the combined nanotherapeutic agents, can achieve the integration of magnetic targeting of tumors under a magnetic field and PTT/PDT synergistic therapy of tumors under low-power laser irradiation. The research not only extends knowledge of PTT/PDT synergetic therapeutic mechanism, but also provides multitudinous possibilities for further development of clinical cancer treatment.

2. Experimental section

Materials, biochemicals and instruments are listed in Supporting Information.

2.1. Fabrication of Au NPs

2 mL of 27.95 mM $HAuCl_4{\cdot}3\,H_2O$ solution was injected into 200 mL of deionized water and stirred magnetically for 150 s. After that, 6 mL of 34 mM trisodium citrate dihydrate was slowly put into mixture and stirred evenly for 200 s. Then, 2 mL of 19.76 mM $NaBH_4$ was rapidly injected under intense magnetic agitation, and the mixed solution turned wine red. Finally, Au NPs were successfully prepared by stirring the mixture for 12 h in the dark.

2.2. Preparation of Fe_3O_4 NPs

1.059 g of iron (III) acetylacetonate, 22.5 mL of dibenzyl ether and 1.95 mL of oleic acid were placed in the two-necked round-bottom flask, respectively. Subsequently, the reactant was degassed by purging with argon for 280 s. Then, the mixed solution was warmed to 300 °C under reflux in argon and maintained for 2 h. After

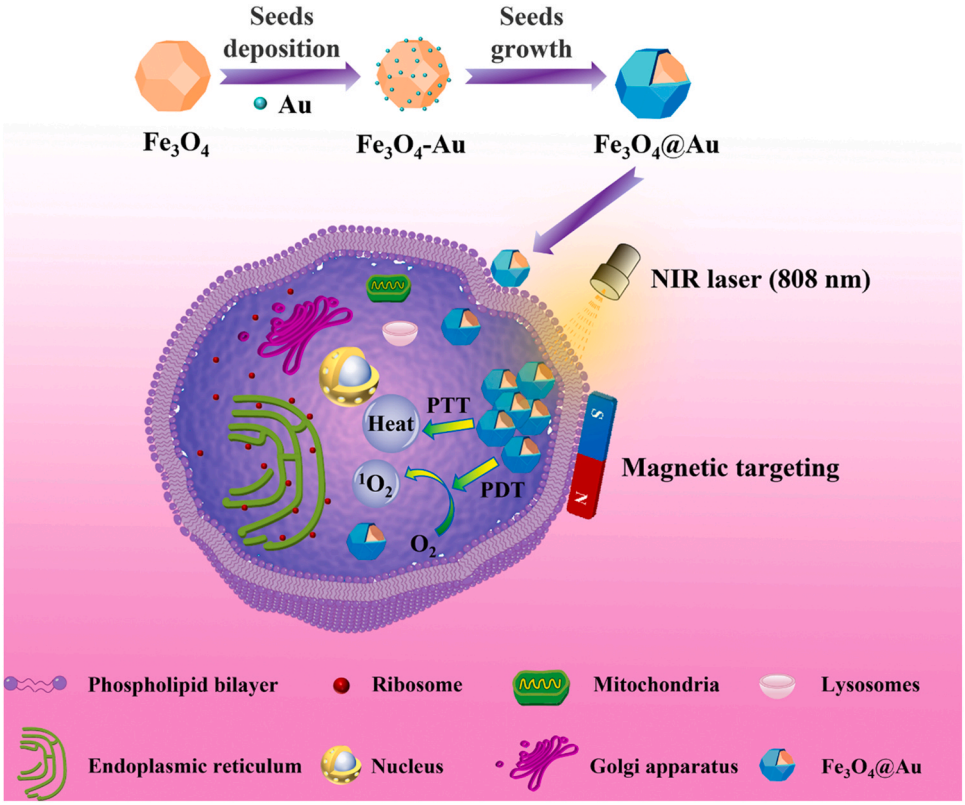

Scheme 1. Schematic representation of preparation process of Fe_3O_4 @Au NCs and their PTT/PDT synergistic targeted treatment for tumors under 808 nm laser irradiation.

reactants were naturally cooled to room temperature, a magnetic field was used externally to collect samples. Final products (Fe_3O_4 NPs) were rinsed several times with mixture of 6.8 mL toluene and 1.7 mL hexane and stored in a vacuum drying oven at 60 °C.

2.3. Synthesis of Fe_3O_4@Au NCs

The synthesis of Fe_3O_4 @Au NCs was divided into three processes. The first step was to functionalize surfaces of Fe_3O_4 NPs with PEI-DTC. Specifically, 0.4875 g of KOH, 0.375 g of PEI and 37.5 mL of methanol were magnetically stirred in a flask until they were completely dissolved. The mixture was degassed for 30 s, and then 521.25 μL of CS_2 was dropped into the flask. After severe agitation for 10 min, the mixed solution became pale yellow, which represented the production of PEI-DTC. Then, 0.015 g of prepared Fe_3O_4 NPs was dissolved in 30 mL of methanol and subsequently put into PEI-DTC solution. After standing for 1 h, the products were rinsed using deionized water and subsequently dissolved in 6 mL of deionized water. The second step was to deposit Au NPs on surfaces of Fe_3O_4 NPs. 120 mL of Au NPs was put into Fe_3O_4 @PEI-DTC solution and ultrasonicated for 2 h. Mixture was rinsed using deionized water to exclude excess Au NPs to obtain Fe_3O_4-Au seeds NCs, and then dispersed in 30 mL of deionized water. The third step was to grow Au shells on the surfaces of Fe_3O_4-Au seeds NCs to achieve the final Fe_3O_4 @Au NCs. 0.249 g of K_2CO_3 and 1.773 mL of 27.95 mM $HAuCl_4 \cdot 3\,H_2O$ solution were added into 150 mL of deionized water under magnetic stirring, respectively. Growth solution was obtained successfully after stirring for 30 min. Finally, 4 mL of Fe_3O_4-Au seeds NCs, 16 mL of growth solution and 20 mL of 40 mM of hydroxylammonium chloride were mixed thoroughly by shaking or vortex. After washing with deionized water, the final products (Fe_3O_4 @Au NCs) were obtained and dried in a vacuum drying oven at 60 °C.

2.4. Photothermal effect and photothermal conversion efficiency (PCE) of Fe_3O_4@Au NCs

Under 808 nm laser irradiation at 1.0 W/cm^2, temperature changes of Fe_3O_4 @Au NCs with various concentrations (10, 25, 50, 100, 150 and 200 μg/mL) in phosphate buffer solution (PBS) were recorded by infrared (IR) thermal imaging camera at 1 min interval. The temperature change curve obtained by irradiating PBS using 808 nm laser was used as control group. Moreover, Fe_3O_4 @Au NCs (100 μg/mL) in PBS were also monitored at various laser power densities (0.5, 0.8, 1.0, 1.3, 1.5, and 1.8 W/cm^2). PCE could be calculated on the basis of following procedure. The Fe_3O_4 @Au NCs in PBS (100 μg/mL) were irradiated using laser of 1.0 W/cm^2 for 10 min. Subsequently, laser was removed and solution was cooled naturally for nearly 20 min. In the above procedure, solution temperature was continuously monitored via IR thermal imaging camera. Finally, PCE was calculated according to method proposed in the literature [58,59].

2.5. Singlet oxygen detection and its reproducibility of Fe_3O_4@Au NCs

Under laser irradiation at 1.0 W/cm^2, singlet oxygen sensor green (SOSG) acted as a probe to investigate $^1O_2$ production of Fe_3O_4 @Au NCs with various concentrations (10, 25, 50, 100, 150 and 200 μg/mL) in PBS. Fluorescence intensity of SOSG procured by irradiating Fe_3O_4 @Au NCs (100 μg/mL) using laser was used as a control. Briefly, SOSG was dispersed in PBS including 2% methanol for achieving a final concentration of 1.0 μM. Then, SOSG was added to the Fe_3O_4 @Au NCs and Fe_3O_4 NPs in PBS, respectively. Fluorescence intensity of mixed solution under laser irradiation was measured every 1 min. Fluorescence intensity of probe molecule SOSG was recorded and their values at 525 nm were plotted against irradiation time. To assess influence of re-irradiation on singlet oxygen generating ability,

Fe_3O_4 @Au NCs (100 μg/mL) were irradiated with 808 nm laser at 1.0 W/cm^2 for diverse times (0, 5, 10 and 15 min). After SOSG was added to those four samples, they were again exposed under laser of 1.0 W/cm^2. Finally, fluorescence intensity of probe molecule SOSG was recorded every 1 min and values of the fluorescence intensity at 525 nm were taken and plotted against irradiation time.

2.6. Cell culture and biocompatibility of Fe_3O_4@Au NCs

The details about cell culture were described in Supporting Information and following experiments were implemented when the cells were stabilized. Fe_3O_4 @Au NCs were dispersed in Dulbecco's minimum essential medium (DMEM) (final concentration of Fe_3O_4 @Au NCs: 0, 20, 50, 100, 200, 300, 400 μg/mL), and they were irradiated with UV light for the purpose of sterilization. Then, 100 μL of aqueous dispersion (Fe_3O_4 @Au NCs) with different concentrations was placed onto the above 96-well plates. Cell viability was measured using 3-(4,5-dimethylthiazol-2-yl)− 2,5-diphenyltetrazolium bromide (MTT) assay after HeLa cells were further cultured for 24 and 48 h. All obtained results were based on three sets of parallel experiments.

2.7. Photocytotoxicity and targeting specificity of Fe_3O_4@Au NCs

After HeLa cells adhered to the wells, Fe_3O_4 @Au NCs with different concentrations (0, 10, 25, 50, 200, 150, 200 μg/mL) in DMEM with or without 0.1 mM of L-ascorbic acid (VC) were placed onto the well plates, and resulting mixed solution was treated with or without a magnetic field for 4 h. Among them, the magnetic field treatment was to place rectangular NdFeB permanent magnets (surface magnetic field of 0.2 T) under the 96-well plate. Subsequently, unbound Fe_3O_4 @Au NCs were removed from the medium through rinsing using PBS. HeLa cells were then treated using laser of 1.0 W/cm^2 for 10 min. Cell viability was evaluated using calcein acetoxymethyl ester/propidium iodide (Calcein-AM/PI) staining and MTT assay. All results were based on three sets of parallel experiments. To explore the effect of magnetic targeting on cellular uptake, Fe_3O_4 @Au NCs labeled with fluorescein isothiocyanate isomer I (FITC) were cultured with HeLa cells for 4 h with/without rectangular NdFeB permanent magnets placed under the 96-well plate. Nuclei were stained with 4′,6-diamidino-2-phenylindole (DAPI), lysosomes were labeled using Lyso-tracker Red, and then cells were rinsed several times using PBS. Cell uptake of Fe_3O_4 @Au NCs was recorded using confocal laser scanning microscopy (CLSM).

3. Results and discussion

3.1. Physicochemical characterizations

SEM is applicable to characterizing morphologies and structures of Fe_3O_4 NPs, Fe_3O_4-Au seeds NCs and Fe_3O_4 @Au NCs, as shown in Fig. 1 **(a)-(c)**. As revealed in Fig. 1 **(a)**, the fabricated Fe_3O_4 NPs have relatively regular shapes and uniform sizes. After immobilizing Au seeds onto Fe_3O_4 NPs, Au seeds are stochastically and uniformly adsorbed on Fe_3O_4 NPs, which can be verified by the SEM image and EDS elemental mapping images in Fig. 1 **(b)**. After treating the Fe_3O_4-Au seeds NCs with reducing agent and growth solution, the amount of Au element increases significantly and the surfaces of Fe_3O_4 NPs are almost completely covered with Au NPs, which basically indicates the formation of core-shell structure, as presented in Fig. 1 **(c)**. XRD patterns displayed in Fig. 1 **(d)** confirm successful synthesis of Fe_3O_4 NPs and Fe_3O_4 @Au NCs. The characteristic diffraction peaks of Fe_3O_4 NPs are located at 2θ = 30.10, 35.42, 37.05, 43.05, 53.39, 56.94, 62.52, 70.92, 73.95 and 74.96°, which correspond to the (220), (311), (222), (400), (422), (511), (440), (620), (533) and (622) planes of Fe_3O_4 (JCPDS No. 19–0629), respectively [60]. As for Fe_3O_4 @Au NCs, four extra diffraction peaks at 2θ = 38.18, 44.39, 64.58, and

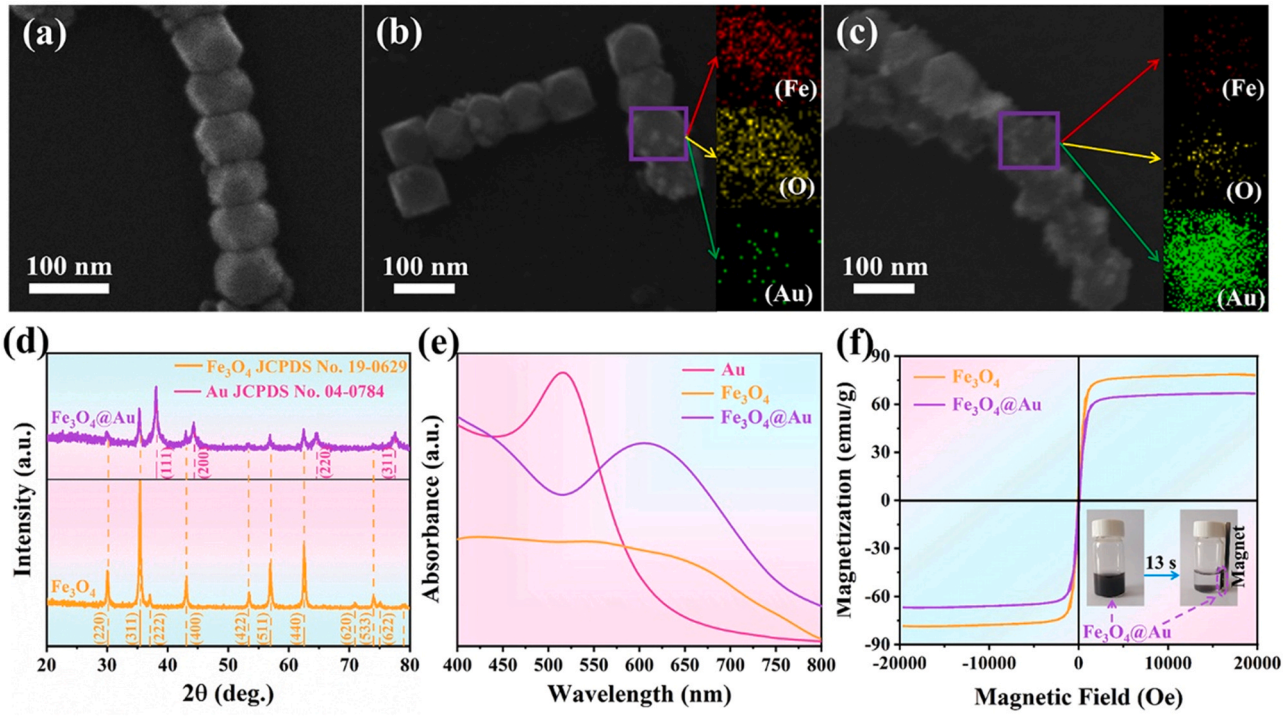

Fig. 1. SEM image of (a) Fe_3O_4 NPs, SEM images of (b) Fe_3O_4-Au seeds NCs and (c) Fe_3O_4 @Au NCs and the corresponding EDS elemental mapping images (Fe, O and Au), (d) XRD patterns, (e) UV-Vis absorption spectra and (f) magnetic hysteresis (*M-H*) loops of Fe_3O_4 NPs and Fe_3O_4 @Au NCs. The photograph of Fe_3O_4 @Au NCs before and after magnetic separation with magnetic field is shown in inset of (f).

77.55° are noticed, which can be pointed to (111), (200), (220) and (311) planes of Au (JCPDS No. 04–0784) [61]. Noticeably, diffraction peak intensity of Fe_3O_4 @Au NCs is significantly reduced compared with that of pure Fe_3O_4 NPs, which indirectly suggests the formation of Au shells on Fe_3O_4 NPs. Fig. 1 **(e)** shows the UV-Vis absorption spectra of Au NPs, Fe_3O_4 NPs and Fe_3O_4 @Au NCs. It is observed that Fe_3O_4 NPs have no evident absorption peak in the range of 400–800 nm. Au NPs exhibit the clear LSPR peak at ~516 nm, which is the typical characteristic of Au nanocrystals [62]. Notably, the LSPR absorption peak of Fe_3O_4 @Au NCs displays a red shift from ~516 to ~610 nm compared with Au NPs, which may be due to electron transfer between Au NPs and Fe_3O_4 NPs [63,64]. In addition, the change in the ratio of the center-to-center distance (L) between Au NPs and the effective diameter (D) of Au NPs may be another reason for the red shift of the LSPR absorption peak of Fe_3O_4 @Au NCs [65,66]. The hysteresis loops of Fe_3O_4 NPs and Fe_3O_4 @Au NCs obtained at room temperature are presented in Fig. 1 **(f)**. The saturation magnetization (Ms) values of Fe_3O_4 NPs and Fe_3O_4 @Au NCs are 78 and 66.5 emu/g, respectively. Although Ms value of Fe_3O_4 @Au NCs decreases due to the diamagnetic contribution from Au shells, they can still be aggregated by nearby magnets within 13 s [67]. It should be highlighted that a nanomaterial with a size between 60 and 400 nm can easily permeate and achieve accumulation in tumor sites because of EPR effect [68,69]. In addition, once a nanomaterial can exhibit a wide light absorption capacity in the range of 600–850 nm, it will show an efficient photothermal conversion ability after the nanomaterial is irradiated with NIR light. More importantly, this wavelength range can be easily absorbed by tissues during PDT treatment and thus reduce the light extinction caused by the inherent chromophores of healthy tissues [43,70]. Given that Fe_3O_4 @Au NCs in this study meet the above conditions, the developed Fe_3O_4 @Au NCs have great potential as PCAs and PSs for achieving NIR-triggered PTT/PDT synergistic therapy.

3.2. Photothermal and photodynamic effect of Fe_3O_4@Au NCs

For the purpose of investigating photothermal effects of Fe_3O_4 @Au NCs, the IR thermal imaging camera was utilized to monitor temperature variations of Fe_3O_4 @Au NCs in PBS. Temperature of all solutions is raised with growth of irradiation time, which is verified by changes in color of solution from blue to red in IR thermal images of Fig. 2 (a). Significantly, the photothermal effects of the Fe_3O_4 @Au NCs are closely related to their concentration, and the photothermal effects are enhanced remarkably when increasing the concentration of Fe_3O_4 @Au NCs. The corresponding time-dependent temperature curves are plotted in Fig. 2 (b). Temperature of Fe_3O_4 @Au NCs (200 μg/mL) rises to 63.8 °C and temperature increment (ΔT) is as high as 34.4 °C within 10 min. The temperature of Fe_3O_4 @Au NCs at 10 μg/mL under laser irradiation can also reach 38 °C within 10 min. By comparison, when PBS acting as control group is irradiated with the same power density, only a small temperature rise of ~3.5 °C is observed, implying that the thermal effect of PBS alone is negligible. In general, local heating of tumor cells to a high temperature > 45 °C can lead to complete tumor eradication. However, excessively high temperature can easily cause the severe side effects to human body, while excessively low temperature will be insufficient to cause tumors ablation and thus result in the recurrence and progression of tumor [71]. Given that the above factors, a concentration of 100 μg/mL is the most appropriate for thermal ablation of tumor cells in this study, because solution temperature is exactly 50.1 °C, which is enough to inactivate tumor cells with little damage to surrounding normal tissues during photothermal treatment of tumors [72]. Furthermore, the photothermal effect of PACs is strongly dependent on power density of laser source [73]. Temperature changes of Fe_3O_4 @Au NCs (100 μg/mL) in PBS at the various laser power densities were presented in Fig. 2 (c) and (d). It can be found that the temperature of Fe_3O_4 @Au NCs in PBS rises continuously with increasing

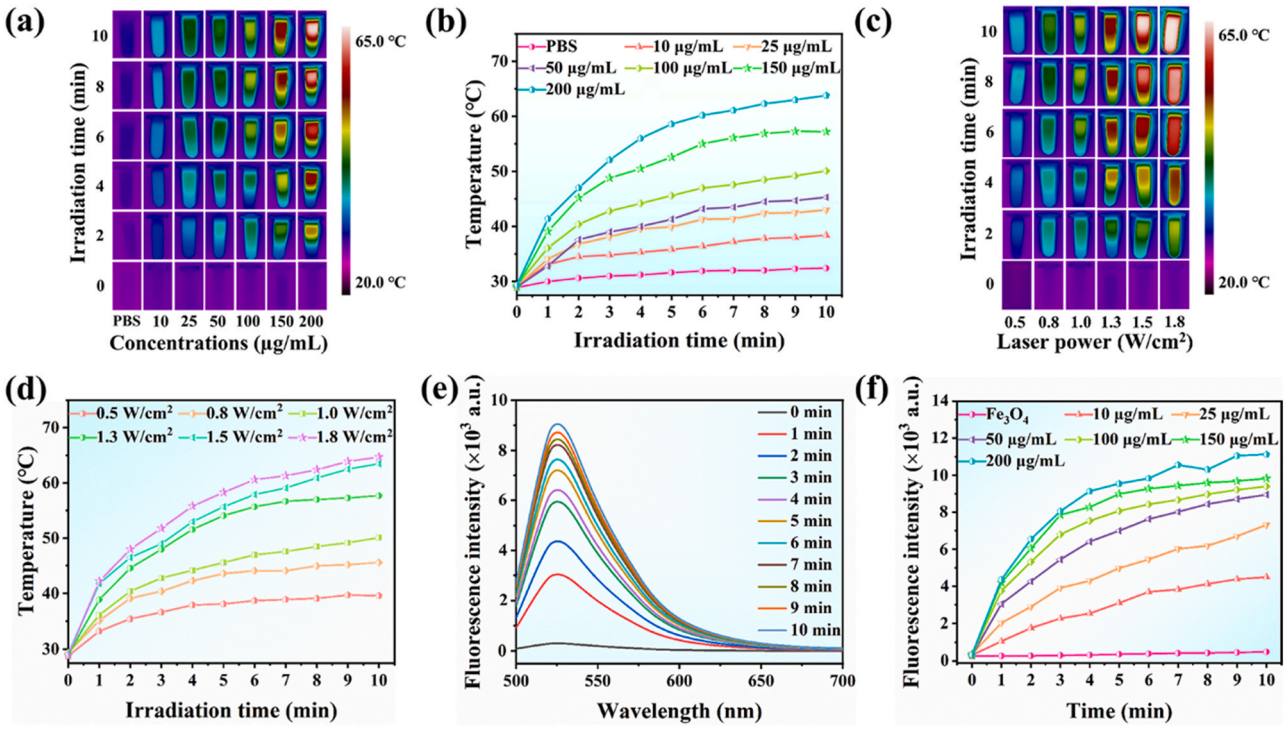

Fig. 2. (a) IR thermal images and (b) corresponding time-temperature curves of PBS and Fe_3O_4 @Au NCs with diverse concentrations (10–200 μg/mL) in PBS under 808 nm laser irradiation at 1.0 W/cm^2, (c) IR thermal images and (d) corresponding time-temperature curves of Fe_3O_4 @Au NCs in PBS (100 μg/mL) at various laser power densities, (e) fluorescence spectra of SOSG in presence of Fe_3O_4 @Au NCs (100 μg/mL) after different irradiation times and (f) time-dependent fluorescence intensity curves of SOSG at 525 nm in presence of Fe_3O_4 NPs (100 μg/mL) and Fe_3O_4 @Au NCs with diverse concentrations.

laser power densities. Although PTT alone can precisely kill the tumor cells through thermal ablation, the combination of PTT with other therapies, especially PDT, is a more efficient way to enhance photothermal efficacy with minimal dosage [74]. Whether Fe_3O_4 @Au NCs can exert a PDT effect depends upon their abilities to generate cytotoxic $^1O_2$ under laser irradiation. Fe_3O_4 @Au NCs are theoretically capable of generating cytotoxic $^1O_2$ owing to the plasmonic electron transfer capacity of Au [75]. In order to prove the above hypothesis, the ability of Fe_3O_4 @Au NCs to generate $^1O_2$ was detected using fluorescent probe (SOSG). It has been validated that SOSG has great selectivity to $^1O_2$ [76]. Once SOSG reacts with $^1O_2$ to produce endoperoxides, the strong fluorescence signals at 525 nm will appear [77,78]. As presented in Fig. 2 (e), the fluorescence intensity observably increases with the increase of time in presence of Fe_3O_4 @Au NCs (100 μg/mL), which is ~18-fold higher than that produced in Fe_3O_4 NPs under same condition (Fig. S1). It implies that Au shells can effectively promote the generation of $^1O_2$ under laser irradiation. Fluorescence intensity and time-dependent fluorescence intensity curves in presence of Fe_3O_4 @Au NCs with various concentrations (10–200 μg/mL) after diverse times of irradiation are exhibited in Fig. 2 **(f)** and **S2**. Fluorescence intensity of SOSG increases as the concentrations of Fe_3O_4 @Au increase from 10 to 200 μg/mL. Such behavior may be explained by an increase of PSs in SOSG. These results suggest that Fe_3O_4 @Au NCs can serve simultaneously as PCAs and PSs to ablate tumor cells.

3.3. Photostability of Fe_3O_4@Au NCs

To further quantify the photothermal conversion capability of Fe_3O_4 @Au NCs, the PCE was assessed by measuring the temperature changes of Fe_3O_4 @Au NCs (100 μg/mL) in PBS under continuous laser irradiation for 10 min (Fig. 3 (a)). The detailed PCE calculation is presented in the Supporting Information. It can be obtained that PCE of Fe_3O_4 @Au NCs (100 μg/mL) in PBS is as high as 39.22%, which is higher than that of the formerly recorded PACs [79–81]. Notably, the corrosion of PCAs is likely to occur in the process of photothermal conversion, thus affecting the conversion efficiency of PCAs [58]. Hence, the photothermal stability of Fe_3O_4 @Au NCs was investigated. Fig. 3 (b) and (c) are IR thermal images and corresponding temperature variations of Fe_3O_4 @Au NCs (100 μg/mL) in PBS under laser irradiation. After six heating and cooling cycles (heating 10 min and cooling 20 min for one cycle), there is remarkably little variation in photothermal conversion performance of Fe_3O_4 @Au NCs. In addition to the photothermal stability, $^1O_2$ regeneration capability of Fe_3O_4 @Au NCs under re-irradiation of 808 nm laser was also evaluated. Fe_3O_4 @Au NCs (100 μg/mL) in PBS were firstly irradiated at various times (0, 5, 10, and 15 min). Subsequently, SOSG was added to the Fe_3O_4 @Au NCs in PBS after laser irradiation, respectively. These four samples were then re-irradiated for additional 10 min and fluorescence intensity of SOSG was recorded every minute (Fig. S3). The changes of fluorescence intensity at 525 nm with time are plotted in Fig. 3 **(d)**. It can be found that the fluorescence intensity increases with increase of time for four samples, and the change trend of the fluorescence intensity is nearly identical, indicating that the ability of Fe_3O_4 @Au NCs to generate $^1O_2$ under re-irradiation is well maintained. Based on the above results, it can be concluded that Fe_3O_4 @Au NCs are promising candidates for next-generation PTT and PDT reagents because of their high PCE and excellent stability.

3.4. Biocompatibility and photocytotoxicity of Fe_3O_4@Au NCs

Given that cervical carcinoma HeLa cells are typically located in the cervix, which is connected to the vagina, it is feasible to treat HeLa cells with laser irradiation and thus HeLa cells were selected as the research object in this work [42,82]. When it comes to cancer therapy, good biocompatibility and low cytotoxicity are the essential prerequisites for ideal nanotherapeutic agents. The biocompatibility

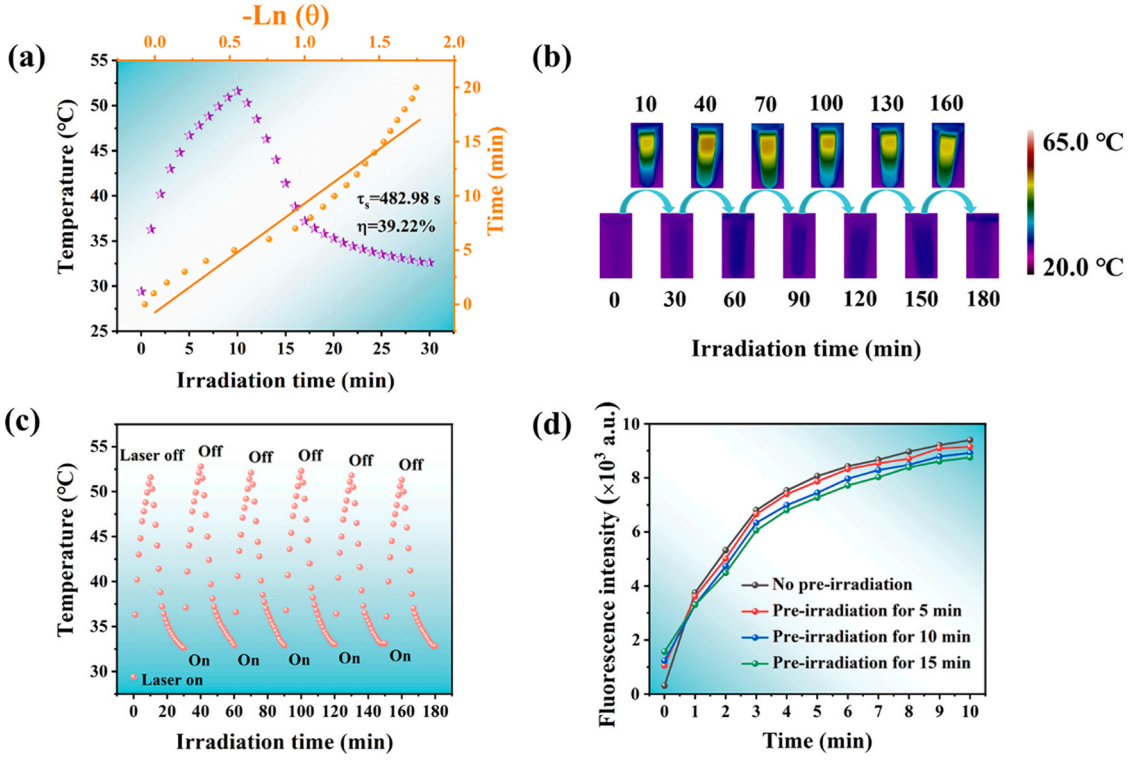

Fig. 3. (a) Calculation of PCE of Fe_3O_4 @Au NCs (100 μg/mL), (b) IR thermal images and (c) corresponding temperature changes of Fe_3O_4 @Au NCs (100 μg/mL) in PBS during six irradiation/cooling cycles (10 min of irradiation for each cycle), (d) changes of fluorescence intensity of SOSG at 525 nm in presence of Fe_3O_4 @Au NCs (100 μg/mL) after re-irradiation.

and in vitro cytotoxicity of prepared Fe_3O_4 @Au NCs were assessed using MTT assay. Fig. 4 **(a)** exhibits cell viability of HeLa cells cultured with different concentrations of Fe_3O_4 @Au NCs in DMEM for 24 and 48 h. A dose-dependent reduction in cell viability is found for both groups. When the concentration of Fe_3O_4 @Au NCs ranges from 10 to 100 μg/mL, cell viability in both groups is higher than 80%. Even at a high concentration of 200 μg/mL and after 48 h incubation, cell viability still remains above 75%, indicating that Fe_3O_4 @Au NCs possess good biocompatibility and low cytotoxicity. In addition, PTT only and PTT/PDT dual-modal therapeutic effect of Fe_3O_4 @Au NCs on HeLa cells were compared. VC was chosen as a scavenger of $^1O_2$ to exclude therapeutic influence of PDT [83]. As shown in Fig. S4, Fe_3O_4 @Au NCs in SOSG exhibit obvious green fluorescence under laser irradiation because of generation of $^1O_2$. By contrast, no obvious fluorescence is observed under the same condition once VC is added (Fig. S5). The result demonstrates that VC can scavenge $^1O_2$ generated by Fe_3O_4 @Au NCs under specific wavelength laser irradiation. Fig. 4 **(b)** exhibits cell viability of HeLa cells incubating with diverse concentrations of Fe_3O_4 @Au NCs (0–200 μg/mL) in DMEM with/without addition of VC and with/without 808 nm laser irradiation. There is no significant change in cell viability with/without addition of VC without laser irradiation, implying that cytotoxicity of VC on HeLa cells is negligible. When 808 nm laser irradiation is carried out, cellular viability of HeLa cells with addition of VC decreases dramatically. Obviously, PTT only presents high therapeutic effect against HeLa cells due to the hyperthermia generated by PCAs from NIR laser energy. Notably, the viability of HeLa cells further decreases without addition of VC under laser irradiation, which can be due to synergistic effect of PTT and PDT. On one hand, the consumption of oxygen during PDT treatment makes cancer cells more sensitive to heat [84]. On the other hand, PTT treatment can promote blood circulation, increase oxygen supply to cancer cells and thus benefit to oxygen-dependent PDT treatment [85]. In addition, the cell viability significantly decreases with increasing dose of Fe_3O_4 @Au NCs. In consideration of the biosafety of the nanotherapeutic agent, the concentration of 100 μg/mL was chosen as ideal dose for following combined PTT/PDT of HeLa cells. The killing ability on Hela cells by combined PTT/PDT of Fe_3O_4 @Au NCs was further verified using staining HeLa cells with Calcein-AM (green) and PI (red). As displayed in Fig. 4 **(c)-(e)**, compared to control group, vast majority of HeLa cells still show green fluorescence after the incubation with Fe_3O_4 @Au NCs only or under10 min of NIR irradiation only, indicating that HeLa cells cannot be effectively inactivated treated either with Fe_3O_4 @Au NCs only or with laser irradiation only. The result directly confirms the low cytotoxicity of Fe_3O_4 @Au NCs and the noninvasiveness of laser irradiation towards cancer cells. By comparison, due to PTT/PDT synergistic effect of Fe_3O_4 @Au NCs, nearly all HeLa cells cultured with Fe_3O_4 @Au NCs are killed under laser irradiation for 10 min, as revealed by intense red fluorescence in Fig. 4 **(f)**. From the results we have obtained from MTT assay and Calcein-AM/PI staining, one can conclude that therapeutic effect of Fe_3O_4 @Au NCs on cancer cells with PDT and PTT synergistic properties is highly efficient.

3.5. Targeting specificity of Fe_3O_4@Au NCs

In order to visualize the cell uptake of multifunctional Fe_3O_4 @Au NCs by HeLa cells and assess the magnetic targeting ability of Fe_3O_4 @Au NCs, Fe_3O_4 @Au NCs, nuclei and lysosomes of HeLa cells were labeled with FITC (green), DAPI (blue) and Lyso-tracker Red (red), respectively, and then characterized by CLSM to track their intracellular distribution with/without an external magnetic field. As illustrated in Fig. 5 **(a)**, green fluorescence represents the Fe_3O_4 @Au NCs labeled with FITC, and blue and red fluorescence are the nuclei and the lysosomes of HeLa cells stained with DAPI and Lyso-tracker Red, respectively. It can be found that the green fluorescence of the Fe_3O_4 @Au NCs shows a high overlap with the blue fluorescence of the nuclei and red fluorescence of the lysosomes even without magnetic field, indicating that Fe_3O_4 @Au NCs are endocytosed by HeLa cells and some of Fe_3O_4 @Au NCs are translocated to inside of HeLa cells. In particular, cell uptake amounts of Fe_3O_4 @Au NCs by HeLa cells increase significantly with an external magnetic field under the same incubation time, as verified by the appearance of stronger fluorescence signals. This result strongly demonstrates that Fe_3O_4 @Au NCs exhibit excellent magnetic targeting ability, which can efficiently promote accumulation at tumor sites and penetration

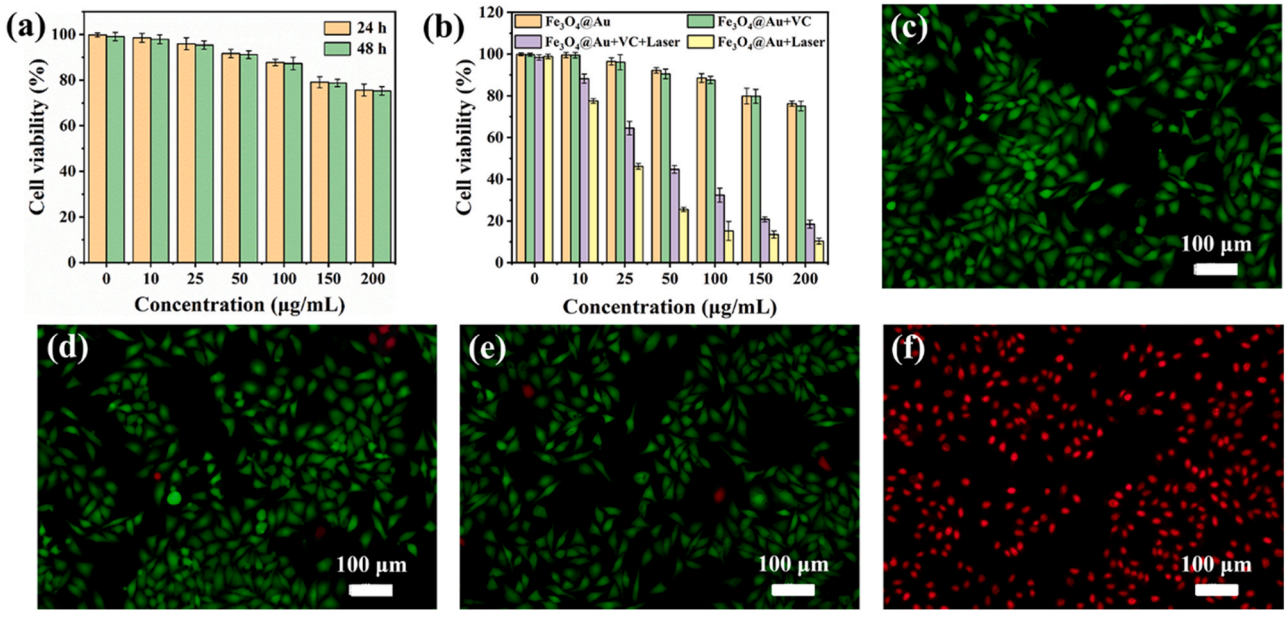

Fig. 4. (a) Cell viability of HeLa cells cultured with different concentrations of Fe_3O_4 @Au NCs (0–200 μg/mL) in DMEM for 24 and 48 h, (b) cell viability of HeLa cells incubating with different concentrations of Fe_3O_4 @Au NCs (0–200 μg/mL) in DMEM with/without addition of VC and with/without laser irradiation for 10 min. Error bars represent the standard deviation from three separate experiments. Fluorescence images of HeLa cells after various treatments: (c) control, (d) 100 μg/mL of Fe_3O_4 @Au NCs in DMEM only, (e) 10 min of NIR irradiation only, and (f) both 100 μg/mL of Fe_3O_4 @Au NCs in DMEM and 10 min of NIR irradiation (808 nm laser, 1.0 W/cm^2).

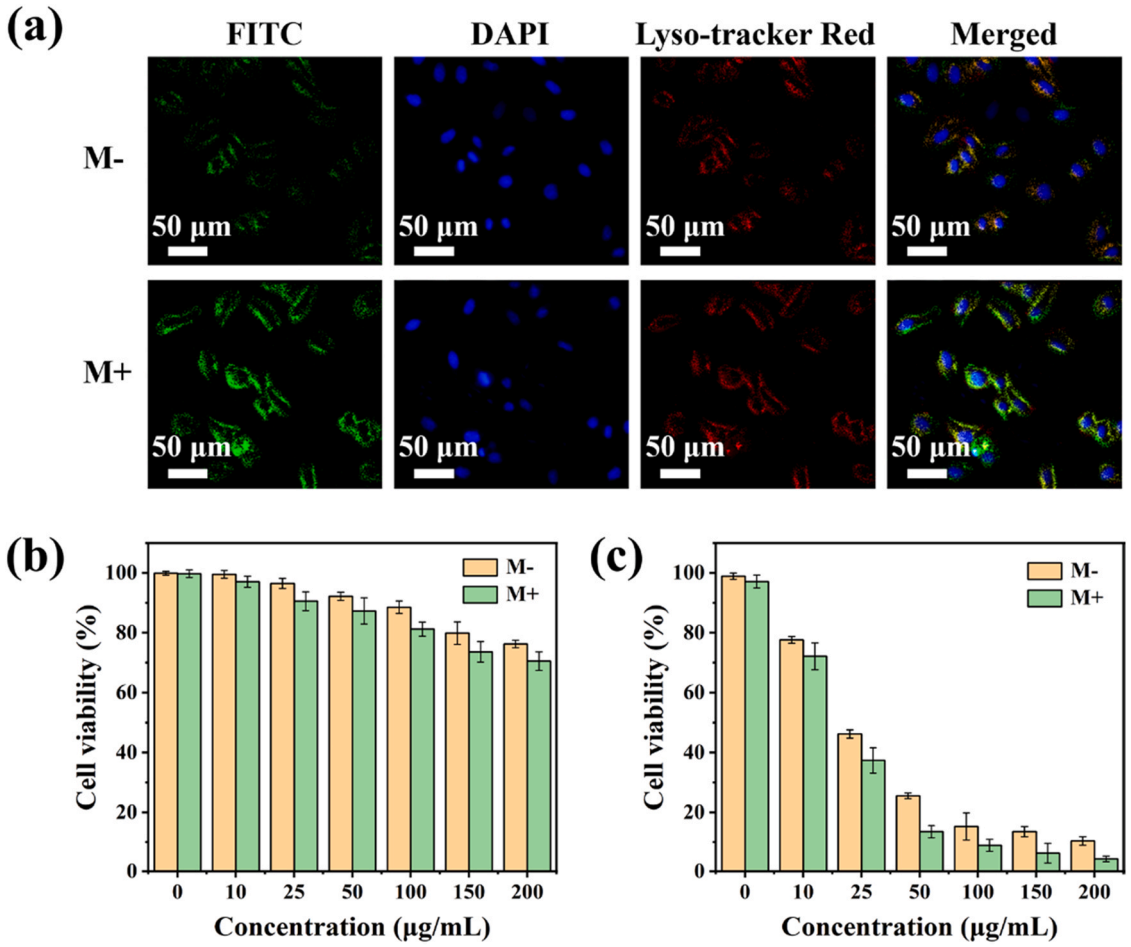

Fig. 5. (a) CLSM images of HeLa cells cultured with Fe_3O_4 @Au NCs labeled with FITC (green). The nuclei are stained with DAPI (blue) and the lysosomes are stained with Lyso-tracker Red (red). Cell viability of HeLa cells cultured with diverse concentrations (0–200 μg/mL) of Fe_3O_4 @Au NCs with/without magnetic field (b) without 808 nm laser irradiation and (c) with 808 nm laser irradiation (10 min, 1.0 W/cm^2). Error bars represent the standard deviation from three separate experiments.

into tumor cells. In addition, the cell viability of HeLa cells cultured with diverse concentrations of Fe_3O_4 @Au NCs with/without magnetic field was measured by MTT assay to explore influence of magnetic targeting on cell viability of HeLa cells. Cell viability of HeLa cells cultured using diverse concentrations of Fe_3O_4 @Au NCs with magnetic field is lower than that of non-magnetically targeting treatment under laser irradiation, as presented in Fig. 5 **(b)**. A possible explanation is that the magnetic targeting can efficiently enhance cellular uptake of Fe_3O_4 @Au NCs and thus lead to a decrease in the cell viability [86]. The role of magnetic targeting in PTT/PDT synergistic therapy was also investigated. As displayed in Fig. 5 **(c)**, once laser irradiation is carried out, cell viability decreases drastically either with or without magnetic field. Notably, the presence of the external magnetic field can induce a comparatively higher cytotoxicity, revealing that the magnetic targeting can further boost PTT/PDT synergistic therapy of tumors owing to EPR effect [57]. These results suggest that the magnetic field-assisted PTT/PDT treatment for cancer therapy is expected to significantly increase the possibility of cell ablation, making it a hopeful strategy for tumor therapies.

4. Conclusion

In summary, the developed Fe_3O_4 @Au NCs had excellent photothermal conversion ability and were capable of generating cytotoxic $^1O_2$ under a single wavelength of laser irradiation, which made it possible to excite PTT and PDT simultaneously with a single laser. In addition, Fe_3O_4 @Au NCs exhibited good photothermal stability and high $^1O_2$ regeneration capability. Surprisingly, even after six heating and cooling cycles, PCE of Fe_3O_4 @Au NCs still remained over 39%. PTT only presented high therapeutic effect on HeLa cells owing to the hyperthermia induced by Fe_3O_4 @Au NCs from NIR laser energy. Notably, simultaneous PTT and PDT generated by Fe_3O_4 @Au NCs under NIR light irradiation exhibited higher therapeutic efficacy on HeLa cells than PTT alone. Furthermore, cell uptake amounts of Fe_3O_4 @Au NCs by HeLa cells increased significantly under the stimulation of external magnetic field, demonstrating that Fe_3O_4 @Au NCs had the excellent magnetic targeting ability. As a result, the combined applications of PTT, PDT and magnetic targeting can efficiently improve treatment of cancer cells. This PTT/PDT synergistic treatment with magnetic targeting capability will afford a concise and efficient strategy for cancer treatment under single-wavelength excitation.

CRediT authorship contribution statement

Tianxiang Zhou: Investigation, Methodology, Formal analysis, Writing – original draft. **Jie Huang:** Investigation. **Wenshi Zhao:** Formal analysis. **Rui Guo:** Conceptualization. **Sicheng Cui:** Data curation. **Yuqing Li:** Visualization. **Naveen Reddy Kadasala:** Validation. **Yuhong Jiang:** Funding acquisition. **Yang Liu:** Conceptualization, Funding acquisition, Writing – review & editing, Supervision. **Qi Zhang:** Supervision.

Data Availability

Data will be made available on request.

Declaration of Competing Interest

The authors declare that they have no known competing financial interests or personal relationships that could have appeared to influence the work reported in this paper.

Acknowledgments

This work was supported by the National Natural Science Foundation of China, China (Grant Numbers 21676115), Program for the Development of Science and Technology of Jilin Province, China (Grant Numbers 20220203021SF, 20200301043RQ and 20200201022JC) and Program for Science and Technology of Education Department of Jilin Province, China (Grant Numbers JJKH20210611KJ and JJKH20220444KJ).

Appendix A. Supporting information

Supplementary data associated with this article can be found in the online version at doi:10.1016/j.jallcom.2023.169206.

References

[1] S. Badrigilan, J. Choupani, H. Khanbabaei, M. Hoseini-Ghahfarokhi, T.J. Webster, L. Tayebi, Bismuth-based nanomaterials: recent advances in tumor targeting and synergistic cancer therapy techniques, Adv. Healthc. Mater. 9 (2020) 1901695.
[2] Y. Guo, Y. Chen, P. Han, Y. Liu, W. Li, F. Zhu, K. Fu, M. Chu, Biocompatible chitosan-carbon nanocage hybrids for sustained drug release and highly efficient laser and microwave co-irradiation induced cancer therapy, Acta Biomater. 103 (2020) 237–246.
[3] H. Sung, J. Ferlay, R.L. Siegel, M. Laversanne, I. Soerjomataram, A. Jemal, F. Bray, Global cancer statistics 2020: GLOBOCAN estimates of incidence and mortality worldwide for 36 cancers in 185 countries, CA-Cancer J. Clin. 71 (2021) 209–249.
[4] E.S. Ali, S.M. Sharker, M.T. Islam, I.N. Khan, S. Shaw, M.A. Rahman, S.J. Uddin, M.C. Shill, S. Rehman, N. Das, S. Ahmad, J.A. Shilpi, S. Tripathi, S.K. Mishra, M.S. Mubarak, Targeting cancer cells with nanotherapeutics and nanodiagnostics: current status and future perspectives, Semin. Cancer Biol. 69 (2021) 52–68.
[5] H. Yang, R. Liu, Y. Xu, L. Qian, Z. Dai, Photosensitizer nanoparticles boost photodynamic therapy for pancreatic cancer treatment, Nano-Micro Lett. 13 (2021) 35.
[6] L.X. Zhang, X.M. Sun, Z.P. Xu, R.T. Liu, Development of multifunctional clay-based nanomedicine for elimination of primary invasive breast cancer and prevention of its lung metastasis and distant inoculation, ACS Appl. Mater. Interfaces 11 (2019) 35566–35576.
[7] S.H. Park, M. Kim, S. Lee, W. Jung, B. Kim, Therapeutic potential of natural products in treatment of cervical cancer: a review, Nutrients 13 (2021) 154.
[8] Z. Xie, T. Fan, J. An, W. Choi, Y. Duo, Y. Ge, B. Zhang, G. Nie, N. Xie, T. Zheng, Y. Chen, H. Zhang, J.S. Kim, Emerging combination strategies with phototherapy in cancer nanomedicine, Chem. Soc. Rev. 49 (2020) 8065–8087.
[9] B. Li, Q. Zhou, H. Wang, Y. Zha, P. Zheng, T. Yang, D. Ma, L. Qiu, X. Xu, Y. Hu, A. Roig, S. Yu, W. Xue, Mitochondria-targeted magnetic gold nanoheterostructure for multi-modal imaging guided photothermal and photodynamic therapy of triple-negative breast cancer, Chem. Eng. J. 403 (2021) 126364.
[10] C. Chu, J. Yu, E. Ren, S. Ou, Y. Zhang, Y. Wu, H. Wu, Y. Zhang, J. Zhu, Q. Dai, X. Wang, Q. Zhao, W. Li, Z. Liu, X. Chen, G. Liu, Multimodal photoacoustic imaging-guided regression of corneal neovascularization: a non-invasive and safe strategy, Adv. Sci. 7 (2020) 2000346.
[11] X. Bao, Y. Yuan, J. Chen, B. Zhang, D. Li, D. Zhou, P. Jing, G. Xu, Y. Wang, K. Hola, D. Shen, C. Wu, L. Song, C. Liu, R. Zboril, S. Qu, In vivo theranostics with near-infrared-emitting carbon dots-highly efficient photothermal therapy based on passive targeting after intravenous administration, Light-Sci. Appl. 7 (2018) 91.
[12] H. Gao, B. Chi, F. Tian, M. Xu, Z. Xu, L. Li, J. Wang, Prussian blue modified metal organic frameworks for imaging guided synergetic tumor therapy with hypoxia modulation, J. Alloy. Compd. 853 (2021) 157329.
[13] J. Chen, C. Ning, Z. Zhou, P. Yu, Y. Zhu, G. Tan, C. Mao, Nanomaterials as photothermal therapeutic agents, Prog. Mater. Sci. 99 (2019) 1–26.
[14] Z. Xie, M. Peng, R. Lu, X. Meng, W. Liang, Z. Li, M. Qiu, B. Zhang, G. Nie, N. Xie, H. Zhang, P.N. Prasad, Black phosphorus-based photothermal therapy with aCD47-mediated immune checkpoint blockade for enhanced cancer immunotherapy, Light-Sci. Appl. 9 (2020) 161.
[15] L. Lin, W. Pang, X. Jiang, S. Ding, X. Wei, B. Gu, Light amplified oxidative stress in tumor microenvironment by carbonized hemin nanoparticles for boosting photodynamic anticancer therapy, Light-Sci. Appl. 11 (2022) 47.
[16] Y. Song, Z. Qu, J. Li, L. Shi, W. Zhao, H. Wang, T. Sun, T. Jia, Y. Sun, Fabrication of the biomimetic DOX/Au@Pt nanoparticles hybrid nanostructures for the combinational chemo/photothermal cancer therapy, J. Alloy. Compd. 881 (2021) 160592.
[17] Z. Wei, F. Xue, F. Xin, M. Wu, B. Wang, X. Zhang, S. Yang, Z. Guo, X. Liu, A thienoisoindigo derivative-based conjugated polymer nanoparticle for photothermal therapy in the NIR-II bio-window, Nanoscale 12 (2020) 19665–19672.
[18] P. Shou, Z. Yu, Y. Wu, Q. Feng, B. Zhou, J. Xing, C. Liu, J. Tu, O.U. Akakuru, Z. Ye, X. Zhang, Z. Lu, L. Zhang, A. Wu, Zn^{2+} doped ultrasmall prussian blue nanotheranostic agent for breast cancer photothermal therapy under MR imaging guidance, Adv. Healthc. Mater. 9 (2020) 1900948.
[19] P. Xu, F. Liang, Nanomaterial-based tumor photothermal immunotherapy, Int. J. Nanomed. 15 (2020) 9159–9180.
[20] J. Yang, D. Dai, X. Lou, L. Ma, B. Wang, Y.W. Yang, Supramolecular nanomaterials based on hollow mesoporous drug carriers and macrocycle-capped CuS nanogates for synergistic chemo-photothermal therapy, Theranostics 10 (2020) 615–629.
[21] Z. Wei, Y. Liu, B. Li, J. Li, S. Lu, X. Xing, K. Liu, F. Wang, H. Zhang, Rare-earth based materials: an effective toolbox for brain imaging, therapy, monitoring and neuromodulation, Light-Sci. Appl. 11 (2022) 175.
[22] S.K. Shaw, J. Kailashiya, S.K. Gupta, C.L. Prajapat, S.S. Meena, D. Dash, P. Maiti, N.K. Prasad, $MnFe_2O_4$ nano-flower: a prospective material for bimodal hyperthermia, J. Alloy. Compd. 899 (2022) 163192.
[23] M. Gorgizadeh, N. Behzadpour, F. Salehi, F. Daneshvar, R.D. Vais, R. Nazari-Vanani, N. Azarpira, M. Lotfi, N. Sattarahmady, A $MnFe_2O_4$/C nanocomposite as a novel theranostic agent in MRI, sonodynamic therapy and photothermal therapy of a melanoma cancer model, J. Alloy. Compd. 816 (2020) 152597.
[24] J. Zhao, L. Duan, A. Wang, J. Fei, J. Li, Insight into the efficiency of oxygen introduced photodynamic therapy (PDT) and deep PDT against cancers with various assembled nanocarriers, WIRES Nanomed. Nanobiotechnol. 12 (2020) e1583.
[25] J.C.S. Simoes, S. Sarpaki, P. Papadimitroulas, B. Therrien, G. Loudos, Conjugated Photosensitizers for Imaging and PDT in Cancer Research, J. Med. Chem. 63 (2020) 14119–14150.
[26] N. Xu, J. Du, Q. Yao, H. Ge, H. Li, F. Xu, F. Gao, L. Xian, J. Fan, X. Peng, Precise photodynamic therapy: Penetrating the nuclear envelope with photosensitive carbon dots, Carbon 159 (2020) 74–82.
[27] E.I. Shramova, S.P. Chumakov, V.O. Shipunova, A.V. Ryabova, G.B. Telegin, A.V. Kabashin, S.M. Deyev, G.M. Proshkina, Genetically encoded BRET-activated photodynamic therapy for the treatment of deep-seated tumors, Light-Sci. Appl. 11 (2022) 38.
[28] J.X. Zhang, W.L. Chan, C. Xie, Y. Zhou, H.F. Chau, P. Maity, G.T. Harrison, A. Amassian, O.F. Mohammed, P.A. Tanner, W.K. Wong, K.L. Wong, Impressive near-infrared brightness and singlet oxygen generation from strategic lanthanide-porphyrin double-decker complexes in aqueous solution, Light-Sci. Appl. 8 (2019) 46.
[29] T.-H. Ho, S.-Y. Hong, C.-H. Yang, Y.-F. Chen, H.-Y. Lin, T.-L. Wang, Preparation of green emission and red emission ligand-free upconverting nanoparticles for investigation of the generation of reactive oxygen species applied to photodynamic therapy, J. Alloy. Compd. 893 (2022) 162323.
[30] Y. Ma, H. Chen, B. Hao, J. Zhou, G. He, Z. Miao, Y. Xu, L. Gao, W. Zhou, Z. Zha, A chloroquine-loaded Prussian blue platform with controllable autophagy inhibition for enhanced photothermal therapy, J. Mater. Chem. B 6 (2018) 5854–5859.
[31] Y. Wang, G. Wei, X. Zhang, X. Huang, J. Zhao, X. Guo, S. Zhou, Multistage targeting strategy using magnetic composite nanoparticles for synergism of photothermal therapy and chemotherapy, Small 14 (2018) 1702994.
[32] B. Li, L. Lin, Internal light source for deep photodynamic therapy, Light-Sci. Appl. 11 (2022) 85.
[33] P. Xi, X. Wei, J. Qu, V.V. Tuchin, Shedding light on biology and healthcare-preface to the special issue on biomedical optics, Light-Sci. Appl. 11 (2022) 156.
[34] P. Sun, X. Wang, G. Wang, W. Deng, Q. Shen, R. Jiang, W. Wang, Q. Fan, W. Huang, A perylene diimide zwitterionic polymer for photoacoustic imaging guided photothermal/photodynamic synergistic therapy with single near-infrared irradiation, J. Mater. Chem. B 6 (2018) 3395–3403.
[35] L. Luo, Z. Wang, Self-assembled $Cu_{2-x}S$ nanochains network with tunable diameters for efficient photothermal conversion, J. Alloy. Compd. 910 (2022) 164958.
[36] M. Li, S. Li, H. Zhou, X. Tang, Y. Wu, W. Jiang, Z. Tian, X. Zhou, X. Yang, Y. Wang, Chemotaxis-driven delivery of nano-pathogenoids for complete eradication of tumors post-phototherapy, Nat. Commun. 11 (2020) 1126.
[37] Z. He, L. Zhao, Q. Zhang, M. Chang, C. Li, H. Zhang, Y. Lu, Y. Chen, An acceptor–donor–acceptor structured small molecule for effective nir triggered dual phototherapy of cancer, Adv. Funct. Mater. 30 (2020) 1910301.
[38] Q. Wan, R. Zhang, Z. Zhuang, Y. Li, Y. Huang, Z. Wang, W. Zhang, J. Hou, B.Z. Tang, Molecular engineering to boost AIE-active free radical photogenerators and enable high-performance photodynamic therapy under hypoxia, Adv. Funct. Mater. 30 (2020) 2002057.
[39] J. Cao, B. Qiao, Y. Luo, C. Cheng, A. Yang, M. Wang, X. Yuan, K. Fan, M. Li, Z. Wang, A multimodal imaging-guided nanoreactor for cooperative combination of tumor starvation and multiple mechanism-enhanced mild temperature phototherapy, Biomater. Sci. 8 (2020) 6561–6578.
[40] W. Shao, C. Yang, F. Li, J. Wu, N. Wang, Q. Ding, J. Gao, D. Ling, Molecular design of conjugated small molecule nanoparticles for synergistically enhanced PTT/PDT, Nano-Micro Lett. 12 (2020) 147.

[41] Z. Tang, P. Zhao, D. Ni, Y. Liu, M. Zhang, H. Wang, H. Zhang, H. Gao, Z. Yao, W. Bu, Pyroelectric nanoplatform for NIR-II-triggered photothermal therapy with simultaneous pyroelectric dynamic therapy, Mater. Horiz. 5 (2018) 946–952.

[42] M.R. Younis, C. Wang, R. An, S. Wang, M.A. Younis, Z.Q. Li, Y. Wang, A. Ihsan, D. Ye, X.H. Xia, Low power single laser activated synergistic cancer phototherapy using photosensitizer functionalized dual plasmonic photothermal nanoagents, ACS Nano 13 (2019) 2544–2557.

[43] M. Azharuddin, G.H. Zhu, D. Das, E. Ozgur, L. Uzun, A.P.F. Turner, H.K. Patra, A repertoire of biomedical applications of noble metal nanoparticles, Chem. Commun. 55 (2019) 6964–6996.

[44] A.K. Mapanao, M. Santi, V. Voliani, Combined chemo-photothermal treatment of three-dimensional head and neck squamous cell carcinomas by gold nano-architectures, J. Colloid Interface Sci. 582 (2021) 1003–1011.

[45] D. Cassano, S. Pocovi-Martinez, V. Voliani, Ultrasmall-in-nano approach: enabling the translation of metal nanomaterials to clinics, Bioconjug. Chem. 29 (2018) 4–16.

[46] N. Hooshmand, A. Thoutam, M. Anikovskiy, H.I. Labouta, M. El-Sayed, Localized surface plasmon resonance as a tool to study protein corona formation on nanoparticles, J. Phys. Chem. C 125 (2021) 24765–24776.

[47] R. Wang, H. Yang, R. Fu, Y. Su, X. Lin, X. Jin, W. Du, X. Shan, G. Huang, Biomimetic upconversion nanoparticles and gold nanoparticles for novel simultaneous dual-modal imaging-guided photothermal therapy of cancer, Cancers 12 (2020) 3136.

[48] W. Sun, L. Luo, Y. Feng, Y. Cai, Y. Zhuang, R.J. Xie, X. Chen, H. Chen, Aggregation-induced emission gold clustoluminogens for enhanced low-dose x-ray-induced photodynamic therapy, Angew. Chem. Int. Ed. 59 (2020) 9914–9921.

[49] R. Kalaivani, M. Maruthupandy, T. Muneeswaran, M. Singh, S. Sureshkumar, M. Anand, C.M. Ramakritinan, F. Quero, A.K. Kumaraguru, Chitosan mediated gold nanoparticles against pathogenic bacteria, fungal strains and MCF-7 cancer cells, Int. J. Biol. Macromol. 146 (2020) 560–568.

[50] T. Zheng, W. Wang, F. Wu, M. Zhang, J. Shen, Y. Sun, Zwitterionic polymer-gated Au@TiO_2 core-shell nanoparticles for imaging-guided combined cancer therapy, Theranostics 9 (2019) 5035–5048.

[51] M.S. Kang, S.Y. Lee, K.S. Kim, D.W. Han, State of the art biocompatible gold nanoparticles for cancer theragnosis, Pharmaceutics 12 (2020) 701.

[52] J. Yu, W. Yin, X. Zheng, G. Tian, X. Zhang, T. Bao, X. Dong, Z. Wang, Z. Gu, X. Ma, Y. Zhao, Smart MoS_2/Fe_3O_4 Nanotheranostic for Magnetically Targeted Photothermal Therapy Guided by Magnetic Resonance/Photoacoustic Imaging, Theranostics 5 (2015) 931–945.

[53] D. Yang, G. Yang, P. Yang, R. Lv, S. Gai, C. Li, F. He, J. Lin, Assembly of Au plasmonic photothermal agent and iron oxide nanoparticles on ultrathin black phosphorus for targeted photothermal and photodynamic cancer therapy, Adv. Funct. Mater. 27 (2017) 1700371.

[54] R. Hu, M. Zheng, J. Wu, C. Li, D. Shen, D. Yang, L. Li, M. Ge, Z. Chang, W. Dong, Core-shell magnetic gold nanoparticles for magnetic field-enhanced radiophotothermal therapy in cervical cancer, Nanomaterials 7 (2017) 111.

[55] R. Guo, H. Peng, Y. Tian, S. Shen, W. Yang, Mitochondria-targeting magnetic composite nanoparticles for enhanced phototherapy of cancer, Small 12 (2016) 4541–4552.

[56] Y. Yang, C. Wang, C. Tian, H. Guo, Y. Shen, M. Zhu, Fe_3O_4@MnO_2@PPy nanocomposites overcome hypoxia: magnetic-targeting-assisted controlled chemotherapy and enhanced photodynamic/photothermal therapy, J. Mater. Chem. B 6 (2018) 6848–6857.

[57] L. Feng, R. Zhao, B. Liu, F. He, S. Gai, Y. Chen, P. Yang, Near-infrared upconversion mesoporous tin oxide bio-photocatalyst for H_2O_2-activatable O_2-generating magnetic targeting synergetic treatment, ACS Appl. Mater. Interfaces 12 (2020) 41047–41061.

[58] M. Ji, M. Xu, W. Zhang, Z. Yang, L. Huang, J. Liu, Y. Zhang, L. Gu, Y. Yu, W. Hao, P. An, L. Zheng, H. Zhu, J. Zhang, Structurally well-defined Au@$Cu_{2-x}S$ core-shell nanocrystals for improved cancer treatment based on enhanced photothermal efficiency, Adv. Mater. 28 (2016) 3094–3101.

[59] Z. Chen, Q. Xia, Y. Zhou, X. Li, L. Qi, Q. Feng, R. Liu, W. Chen, 2-Dicyanomethylenethiazole based NIR absorbing organic nanoparticles for photothermal therapy and photoacoustic imaging, J. Mater. Chem. B 7 (2019) 3950–3957.

[60] W. Zhao, S. Yang, C. Guo, J. Yang, Y. Liu, One-step fabrication of Fe_3O_4-Cu nanocomposites: High-efficiency and low-cost catalysts for reduction of 4-nitrophenol, Mater. Chem. Phys. 260 (2021) 124144.

[61] T. Wu, H. Zheng, Y. Kou, X. Su, N.R. Kadasala, M. Gao, L. Chen, D. Han, Y. Liu, J. Yang, Self-sustainable and recyclable ternary Au@Cu_2O-Ag nanocomposites: application in ultrasensitive SERS detection and highly efficient photocatalysis of organic dyes under visible light, Microsyst. Nanoeng. 7 (2021) 23.

[62] N. Cathcart, J.I.L. Chen, V. Kitaev, L.S.P.R. Tuning, from 470 to 800 nm and improved stability of Au-Ag nanoparticles formed by gold deposition and rebuilding in the presence of poly(styrenesulfonate), Langmuir 34 (2018) 612–621.

[63] L. Wang, J. Luo, Q. Fan, M. Suzuki, I.S. Suzuki, M.H. Engelhard, Y. Lin, N. Kim, J.Q. Wang, C.-J. Zhong, Monodispersed core-shell Fe_3O_4@Au nanoparticles, J. Phys. Chem. B 109 (2005) 21593–21601.

[64] C. Karami, M.A. Taher, A catechol biosensor based on immobilizing laccase to Fe_3O_4@Au core-shell nanoparticles, Int. J. Biol. Macromol. 129 (2019) 84–90.

[65] L. Yang, H. Wang, B. Yan, B.M. Reinhard, Calibration of silver plasmon rulers in the 1–25 nm separation range: experimental indications of distinct plasmon coupling regimes, J. Phys. Chem. C 114 (2010) 4901–4908.

[66] S. Zhang, W. Ni, X. Kou, M.H. Yeung, L. Sun, J. Wang, C. Yan, Formation of gold and silver nanoparticle arrays and thin shells on mesostructured silica nanofibers, Adv. Funct. Mater. 17 (2007) 3258–3266.

[67] X. Wang, H. Liu, D. Chen, X. Meng, T. Liu, C. Fu, N. Hao, Y. Zhang, X. Wu, J. Ren, F. Tang, Multifunctional Fe_3O_4@P(St/MAA)@chitosan@Au core/shell nanoparticles for dual imaging and photothermal therapy, ACS Appl. Mater. Interfaces 5 (2013) 4966–4971.

[68] W.T. Chen, S.T. Kang, J.L. Lin, C.H. Wang, R.C. Chen, C.K. Yeh, Targeted tumor theranostics using folate-conjugated and camptothecin-loaded acoustic nanodroplets in a mouse xenograft model, Biomaterials 53 (2015) 699–708.

[69] H. Liu, D. Chen, F. Tang, G. Du, L. Li, X. Meng, W. Liang, Y. Zhang, X. Teng, Y. Li, Photothermal therapy of Lewis lung carcinoma in mice using gold nanoshells on carboxylated polystyrene spheres, Nanotechnology 19 (2008) 455101.

[70] W. Wei, X. Zhang, S. Zhang, G. Wei, Z. Su, Biomedical and bioactive engineered nanomaterials for targeted tumor photothermal therapy: a review, Mater. Sci. Eng. C 104 (2019) 109891.

[71] W. Yang, J. Noh, H. Park, S. Gwon, B. Singh, C. Song, D. Lee, Near infrared dye-conjugated oxidative stress amplifying polymer micelles for dual imaging and synergistic anticancer phototherapy, Biomaterials 154 (2018) 48–59.

[72] M. Ding, K. Shao, L. Wu, Y. Jiang, B. Cheng, L. Wang, J. Shi, X. Kong, A NO/ROS/RNS cascaded-releasing nano-platform for gas/PDT/PTT/immunotherapy of tumors, Biomater. Sci. 9 (2021) 5824–5840.

[73] P. Chen, Y. Ma, Z. Zheng, C. Wu, Y. Wang, G. Liang, Facile syntheses of conjugated polymers for photothermal tumour therapy, Nat. Commun. 10 (2019) 1192.

[74] H. Liu, J. Zhang, Y. Jia, X. Liu, X. Chen, W. Zhao, C. Mao, Theranostic nanomotors for tumor multimode imaging and photothermal/photodynamic synergistic therapy, Chem. Eng. J. 442 (2022) 135994.

[75] W. Wang, C. Hao, M. Sun, L. Xu, C. Xu, H. Kuang, Spiky Fe_3O_4@Au supraparticles for multimodal in vivo imaging, Adv. Funct. Mater. 28 (2018) 1800310.

[76] R. Vankayala, A. Sagadevan, P. Vijayaraghavan, C.L. Kuo, K.C. Hwang, Metal nanoparticles sensitize the formation of singlet oxygen, Angew. Chem. Int. Ed. 50 (2011) 10640–10644.

[77] J. Zou, J. Zhu, Z. Yang, L. Li, W. Fan, L. He, W. Tang, L. Deng, J. Mu, Y. Ma, Y. Cheng, W. Huang, X. Dong, X. Chen, A. Phototheranostic, Strategy to continuously deliver singlet oxygen in the dark and hypoxic tumor microenvironment, Angew. Chem. Int. Ed. 59 (2020) 8833–8838.

[78] X. Cui, J. Zhang, Y. Wan, F. Fang, R. Chen, D. Shen, Z. Huang, S. Tian, Y. Xiao, X. Li, J. Chelora, Y. Liu, W. Zhang, C.S. Lee, Dual fenton catalytic nanoreactor for integrative type-I and type-II photodynamic therapy against hypoxic cancer cells, ACS Appl. Bio Mater. 2 (2019) 3854–3860.

[79] M. Chang, M. Wang, M. Shu, Y. Zhao, B. Ding, S. Huang, Z. Hou, G. Han, J. Lin, Enhanced photoconversion performance of $NdVO_4$/Au nanocrystals for photothermal/photoacoustic imaging guided and near infrared light-triggered anticancer phototherapy, Acta Biomater. 99 (2019) 295–306.

[80] L. Yang, B. Hu, A.-H. Liu, Y. Zhang, A hollow-structured nanohybrid: Intelligent and visible drug delivery and photothermal therapy for cancer, Talanta 215 (2020) 120893.

[81] F. Gao, M. Sun, L. Xu, L. Liu, H. Kuang, C. Xu, Biocompatible cup-shaped nanocrystal with ultrahigh photothermal efficiency as tumor therapeutic agent, Adv. Funct. Mater. 27 (2017) 1700605.

[82] M.M. Liu, R.H. Ma, Z.J. Ni, K. Thakur, C.L. Cespedes-Acuna, L. Jiang, Z.J. Wei, Apigenin 7-O-glucoside promotes cell apoptosis through the PTEN/PI3K/AKT pathway and inhibits cell migration in cervical cancer HeLa cells, Food Chem. Toxicol. 146 (2020) 111843.

[83] R.S. Bodaness, P.C. Chan, Ascorbic acid as a scavenger of singlet oxygen, FEBS Lett. 105 (1979) 195–196.

[84] X. Ouyang, X. Wang, H.B. Kraatz, S. Ahmadi, J. Gao, Y. Lv, X. Sun, Y. Huang, A. Trojan, horse biomimetic delivery strategy using mesenchymal stem cells for PDT/PTT therapy against lung melanoma metastasis, Biomater. Sci. 8 (2020) 1160–1170.

[85] S. Li, W. Zhang, H. Xue, R. Xing, X. Yan, Tumor microenvironment-oriented adaptive nanodrugs based on peptide self-assembly, Chem. Sci. 11 (2020) 8644–8656.

[86] Q. Fu, Z. Li, J. Ye, Z. Li, F. Fu, S.L. Lin, C.A. Chang, H. Yang, J. Song, Magnetic targeted near-infrared II PA/MR imaging guided photothermal therapy to trigger cancer immunotherapy, Theranostics 10 (2020) 4997–5010.